Structure–Phase Characteristics and the Mechanical Properties of Single-Crystal Nickel-Based Rhenium-Containing Superalloys with Carbide–Intermetallic Hardening

N. V. Petrushin, E. M. Visik, M. A. Gorbovets, and R. M. Nazarkin

All-Russia Scientific Research Institute of Aviation Materials VIAM, ul. Radio 17, Moscow, 105005 Russia
e-mail: admin@viam.ru
Received October 19, 2015

Abstract—Single crystals of rhenium-containing ZhS32-VI, ZhS32U nickel superalloys with the ⟨001⟩, ⟨011⟩, and ⟨111⟩ crystallographic orientations have been produced by directional solidification. The alloying element segregations and the thermal stability of the microstructure consisting of a γ solid solution and hardened by precipitates of the γ′ phase and MC carbides are studied. The crystal lattice parameters of the γ′ and γ phases; the γ/γ′ misfit; and the liquidus, solidus, and γ′-solvus temperatures of the alloys have been found. The temperature dependence of the γ′-phase solubility has beeisn determined. The temperature–orientation dependences of the tensile strength characteristics in the range 20–1150°C and the low-cycle fatigue at 850°C of the alloy single crystals with the ⟨001⟩, ⟨011⟩, and ⟨111⟩ orientations are presented.

INTRODUCTION

As a result of the tendency to enhance the high-temperature properties of alloys by alloying, a cast ZhS32 nickel-based superalloy (NS) containing up to 4 wt % Re was designed at VIAM in the mid-1980s [1]. Since the rhenium-containing ZhS32 superalloy alloyed with a traditional set of elements (Al, Cr, Co, Mo, W, Ta, Nb) contained carbon, it had a three-phase γ + γ′ + MC structure (here, γ is a fcc disordered nickel solid solution, γ′ is an Ni₃Al intermetallic compound-based phase, and MC is a tantalum-based carbide phase). The commercial ZhS32-VI (vacuum-induction melting) superalloy designed almost ten years before similar foreign alloys is widely used to produce turbine blades with columnar and single-crystal structures for aviation gas-turbine engines using directional solidification [2].

Table 1 gives the chemical composition and the density of the ZhS32 alloy and other well-known commercial nickel rhenium-containing superalloys with carbide–intermetallic hardening René N5 [3, 4] and CM186LC [5–7]. Note that the ZhNS alloys containing 2–4 wt % Re belong to second-generation alloys, according to an international classification. Table 2 gives, for comparison, the long-term strengths of these NSs. The results demonstrate an advantage of the ZhS32 superalloy in long-term strength and temperature working capacity, which is mainly a result of rhenium alloying.

Rhenium belongs to the elements that most effectively harden single-crystal NSs [9, 10]. The rhenium distribution ratio between the γ′ phase and the equilibrium γ solid solution is ~0.1, which is significantly lower than those of all other alloying elements. The predominant distribution of rhenium in the γ solid solution substantially decreases the rate of the diffusion processes controlling high-temperature creep (rhenium significantly increases the solidus temperature of nickel superalloys). However, when NSs are not balanced in the concentrations of a number of

Table 1. Chemical composition and density of nickel-based rhenium-containing alloys with carbide–intermetallic hardening [2–7]

Alloy	Alloying element content, wt %											ρ, g/cm³
	Al	Cr	Co	Mo	Ta	W	Re	Nb	Hf	C	Others	
ZhS32	5.9	4.9	9.0	1.0	4.0	8.5	4	1.6	—	0.15	0.015B	8.8
René N5	6.2	7.0	7.5	1.5	6.5	5.0	3	—	0.15	0.05	0.004B	8.6
CM186LC	5.7	6.0	9.0	0.5	3.0	8.0	3	—	1.40	0.07	0.7Ti; 0.005Zr	8.7

alloying elements (Cr, Mo, W, Re), they manifest a tendency to form topologically close-packed (TCP) phases, such as σ, P/R, and μ, at high temperatures [11]. Most of TCP phases decrease the short-time and the long-term mechanical characteristics of NSs, since they are brittle and also take the refractory elements that harden a nickel γ matrix effectively from it. Here, it should be noted that the presence of carbon in the alloys accelerates the solid-phase reactions with formation of M_6C-type carbides, which have structures close to that of the TCP μ phase [12]. In this regard, the removal of carbon and, therefore, carbide phases from the compositions of single-crystal NSs made it possible to increase the phase stability of NSs and their solidus temperatures, long-term strengths, mechanical and thermal fatigue resistances [13]. However, the practice of production of turbine single-crystal blades with complex geometric shapes, in particular, large-scale blades, in industrial directional solidification units showed that subgrains can locally form in some elements of turbine blade ingots (platforms, foot) [14].

Because of this, small amounts of carbon and other horophilic additives are introduced in NSs intended for casting of such blades to harden low-angle subgrain boundaries in them [3, 5, 15].

The development of technologies of rhenium-containing NSs and casting of single-crystal blades is the most important factor of solving the problem of designing high-efficient aviation gas-turbine engines [16]. The main advantages of single-crystal blades are a high high-temperature creep resistance, a high thermal fatigue due to a single-crystal structure (the absence of grain boundaries), and a lower elastic modulus in the ⟨001⟩ crystallographic direction as compared to that of polycrystalline blades of equiaxial solidification [13]. Unlike the properties of polycrystalline isotropic materials, the mechanical properties of single-crystal NSs are dependent on the crystallographic directions along which these properties are determined. The mechanical properties of NS single crystals were studied over a wide temperature range in detail. First of all, the short-time and long-term strengths were studied. The cyclic strength, namely, the low-cycle fatigue (LCF) as one of the most significant parameters in calculating the resource of single-crystal blades, has not been adequately studied.

The aim of this work is to study the structure–phase characteristics (phase composition, segregation coefficient, phase transformation temperatures, solubility of the γ′ phase, lattice parameters of the γ′ and γ phases); the thermal stability of a microstructure; and the temperature–orientation dependence of the strength, the ductility, and the low-cycle fatigue of single-crystal rhenium-containing NSs with carbide–intermetallic hardening.

Table 2. Long-term strength of ⟨001⟩ single crystals of rhenium-containing NSs with carbide–intermetallic hardening

Alloy	T, °C	σ_{100}	σ_{500}	σ_{1000}	Source
		MPa			
ZhS32	900	475	370	330	[8]
	1000	240	175	155	
	1100	120	90	75	
René N5*	900	435	360	320	[4]
	1000	225	160	140	
	1100	110	—	—	
CM186LC*	900	420	340	300	[7]
	1000	210	125	—	

* We obtained the long-term strength by processing the data in [4–7] using the Larson–Miller parametric dependence.

EXPERIMENTAL

We studied single crystals of rhenium-containing nickel ZhS32-VI superalloy with the composition (wt %) Ni–6% Al–4.8% Cr–9.5% Co–1.2% Mo–4% Ta–8.4% W–3.9% Re–1.5% Nb–0.12% C–0.015% B and the ZhS32U superalloy with carbide–intermetallic hardening. Compared to the ZhS32-VI superalloy, the ZhS32U superalloy has lower contents of tungsten (7.2 wt %), niobium (0.8 wt %), and carbon (0.08 wt %).

Single-crystal ingots of the specimens (15 mm in diameter and ~180 mm in length) of these alloys were produced in an UVNK-9A industrial unit for directional solidification by the liquid metal cooling (LMC) method at a solidification rate of 0.7 cm/min and an axial temperature gradient of ~60°C/cm at the growth front [17]. In this case, to form a single-crystal structure of specimen ingots with a given crystallographic orientation (CGO), we used special seed single crystals (seeds) of an Ni–W alloy with the melting temperature that was ~160°C higher than the solidus temperature of the superalloy. The seed casting technology made it possible to produce cylindrical single-crystal ingots of the ZhS32-VI and ZhS32U superalloys with the ⟨001⟩, ⟨011⟩, and ⟨111⟩ CGOs in the axial direction. The crystallographic orientation of the single-crystal ingots was determined by X-ray diffraction (XRD) using a DRON-3 X-ray diffractometer.

The solidus and liquidus temperatures of the superalloys and the temperatures of the onset and complete dissolution of the γ′ phase in a matrix γ solid solution (γ solvus) were found by differential thermal analysis (DTA) using a DSC PT 1750 differential scanning calorimeter. Specimens 4 mm in diameter and 1 mm in length were heated at a constant rate of 20°C/min in a helium atmosphere. The temperature stability of the solubility of the γ′ phase in the superalloys was determined by calculations using the characteristic temperatures (the temperatures of the start and complete dissolution of the γ′ phase) and the volume fraction of
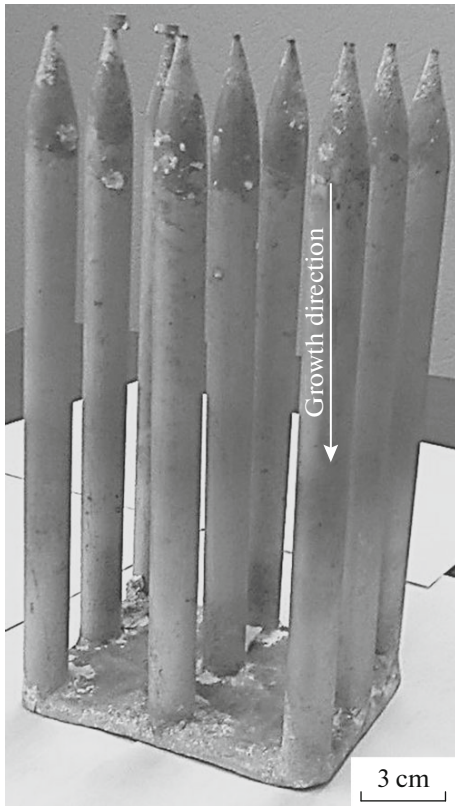
Growth direction

3 cm

Fig. 1. Block of single-crystal ingots of samples.

the γ′ phase at room temperature $F_{0_{γ'}}$ %, which was calculated using the regression equation [18]

$$F_{0_{γ'}} = 14.7 + 0.54[Al] + 1.07[Cr]$$
$$- 1.27[Mo] + 0.23[W] + 4.96[Ta]$$
$$+ 0.31[Co] + 2.54[Nb] + 3.81[Ti] \qquad (1)$$
$$- 0.75[Re] - 3.11[V] + 1.87[Hf]$$
$$- 1.91[C] + 0.17[Al]^2 - 0.08[Cr]^2.$$

In the square brackets of Eq. (1), the element contents are given in at %.

The thermal stability of the alloy microstructure was studied using isothermal annealing at temperatures of 1150 and 1280°C; the annealing times were 660 and 4 h, respectively.

Microstructural studies were performed with a JSM-6490LV scanning electron microscope, and the local chemical composition was determined by electron-probe microanalysis (EPMA) on a JSMA-733 microanalyzer.

X-ray diffraction patterns for structural analysis of the γ/γ′ substructure were taken on a PAnalytical EMPYREAN X-ray diffractometer using the (222) reflection of CuKα radiation. X-ray diffraction patterns were taken from the plane perpendicular to the solidification axis of a single-crystal specimen. XRD

structural analysis was carried out using the Data Collector, Data Viewer, and High Score computer programs, and the separation of the summary (γ + γ′) profile of $Kα_1$ into singlets of the γ and γ′ phases was performed using the pseudo-Voigt function. The lattice misfit of the phases Δa (γ/γ′ misfit) was calculated by the formula

$$\Delta a = (a_γ - a_{γ'})/a_{γ'}, \qquad (2)$$

where $a_γ$ and $a_{γ'}$ are the lattice parameters of the γ solid solution and the γ′ phase, respectively.

The specimens for studying the mechanical properties were prepared from the single-crystal ingots, in which the longitudinal axis coincided (within 10°) with one of the ⟨001⟩, ⟨011⟩, and ⟨111⟩ crystallographic directions. Before preparing the specimens, the ingots were subjected to heat treatment consisting of homogenization and two-step aging. To exclude local melting of interdendrite portions, the homogenization temperature was chosen to be lower than the temperature of the eutectic (peritectic) transformation $L \to γ' + γ$ ($L + γ \to γ'$). The final operation of preparing the specimens was longitudinal polishing of their gage parts.

The tensile tests of the single-crystal samples (gage part was 5 mm in diameter and 25 mm in length) were performed by a standard method (according to GOST 1497 and GOST 9651) in the temperature range 20–1150°C to determine the short-time strength and plasticity characteristics.

The low-cycle fatigue tests were carried out according to GOST 25.502 and ASTM E606 using Walter + Bai LFV100 testing machines during uniaxial tension–compression under conditions of controlling the strain of the gage portion (hard loading) upon asymmetric loading with a stress ratio $R_ε = 0$ at a frequency of 0.5 Hz. The loading cycle was triangular, the controlled parameter during loading was peak-to-peak strain Δε in a cycle, and the test temperature was 850°C. Smooth cylindrical specimens (gage portion was 5 mm in diameter and 15 mm in length) were used. The technique of LCF tests was described in more detail in [19]. The statistical treatment of the test results was performed using the exponential dependence [20]

$$N = B\exp(-β\Delta ε), \qquad (3)$$

where N is the number of fracture cycles and B and β are coefficients found from the test results.

RESULTS AND DISCUSSION

Microstructures and the Phase Compositions of the Superalloys

The single-crystal superalloys produced by directional solidification (Fig. 1) had a dendritic–cellular structure with a distance of 250–280 μm between first-order dendrite axes, which is independent of
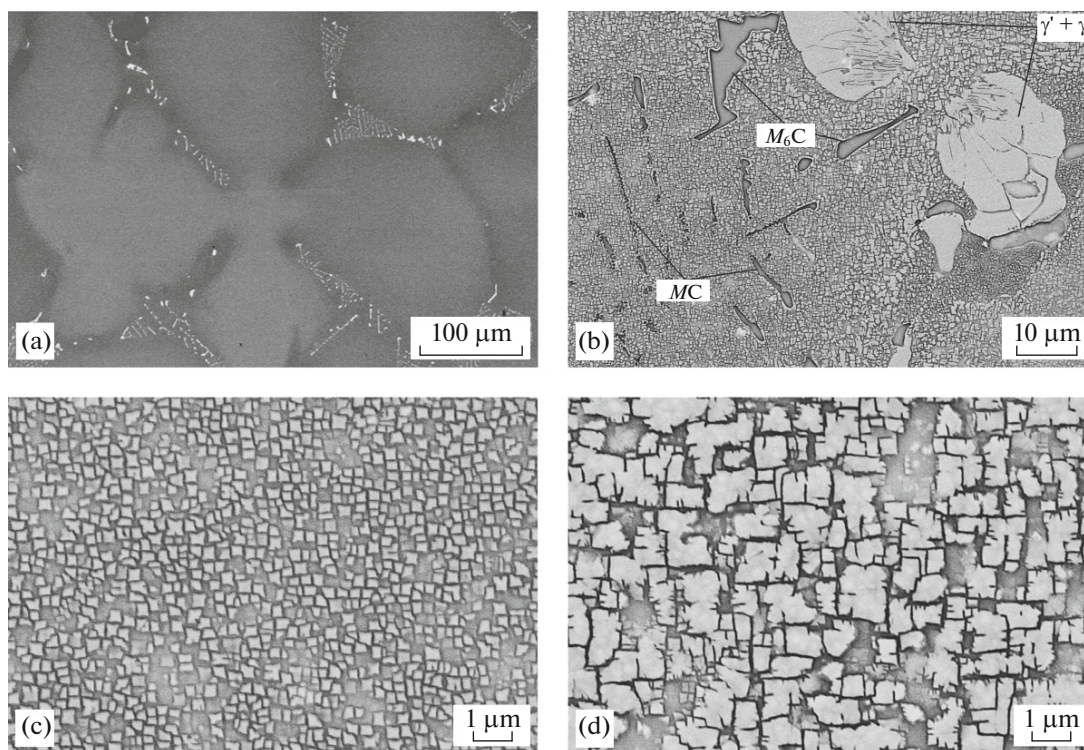
Fig. 2. Microstructure of the cast ZhS32-VI superalloy ⟨001⟩ single crystal (cross sections): (a) dendritic–cellular structure, (b) eutectic (peritectic) γ′ phase and carbide phases in the interdendrite region, and (c, d) γ′-phase particles in (c) primary γ dendrite arm matrix and (d) interdendrite region.

CGO (Fig. 2a). The superalloy structure consists of the matrix γ phase (nickel γ solid solution) and precipitates of the γ′ phase based on the Ni_3Al intermetallic compound. The γ′-phase precipitates were dispersed particles disposed in the γ matrix of dendrite arms and interdendrite regions and coarse eutectic (peritectic) particles occurring between secondary dendrite arms (Figs. 2b–2d). According to the DTA data, the eutectic (peritectic) γ phase forms at a temperature of 1310–1315°C at the end of solidification of remaining melt in interdendrite regions; the chemical composition of this phase is given in Table 3.

Figure 2b shows that the interdendrite regions of the single crystals contain lamellar phase precipitates. According to the EPMA data, the thin plates of these precipitates are MC-type carbides (Table 3, carbide phase 1). Coarse lamellar particles visible in Fig. 2b near the eutectic (peritectic) γ phase are enriched in rhenium, tungsten, molybdenum, and chromium. According to the chemical composition, these particles should be referred to MC carbides (Table 3, carbide phase 2). The DTA data showed that the carbide phases form during solidification beginning from temperatures of 1346°C in the ZhS32-VI superalloy and of 1374°C in the ZhS32U superalloy. Note that M_6C carbides were not detected in the structure of as-cast ZhS32U superalloy single crystals.

The γ′-phase particles in the as-cast single crystals of the ZhS32-VI and ZhS32U alloys had significantly different sizes and shapes in the materials of dendrites and interdendrite regions; in these regions, the γ′-phase particles were coarser (Figs. 2c, 2d).

The observed size inhomogeneity of the γ′-phase particles and the existence of precipitations of the eutectic (peritectic) γ′-phase in the cast single crystals of the alloys are due to the segregation of alloying elements within dendrite cells during directional solidification. Dendrite segregation is quantitatively characterized by the segregation coefficient [21]

$$K_s = n(C_{id}/C_{da})^n, \qquad (4)$$

where C_{id} and C_{da} are the element concentrations in dendrite portions and the primary dendrite arms, respectively, and $n = \pm 1$ is a coefficient.

An analysis of Eq. (4) showed that, if $C_{id} > C_{da}$, we have $n = +1$ and $K_s = C_{id}/C_{da} > 1$. In this case, segregation is considered to be "forward." When alloying elements are concentrated in dendrite arms ($C_{id} < C_{da}$), we have $n = -1$ and $K_s = -(C_{da}/C_{id}) < -1$. In this case, segregation is considered to be "inverse."

Table 4 gives the typical local chemical composition of the γ/γ′ matrix in primary dendrite arms and the interdendrite portions and also the dendrite segregation coefficients of the alloying elements for the

Table 3. Chemical composition* of the eutectic (peritectic) γ′ and carbide phases in the as-cast and heat-treated single crystals of the ZhS32-VI superalloy

Object of analysis	Element content, wt %									Σ, wt %
	Al	Cr	Co	Ni	Mo	Nb	Ta	W	Re	
As-cast alloy specimens										
Eutectic (peritectic) γ′ phase	8.7	3.1	8.4	65.1	0.5	2.4	6.7	4.2	0.8	99.9
Carbide phases:										
1	0.1	0.8	1.0	5.6	1.2	25.3	56.6	5.7	–	96.3
2	0.7	9.4	11.5	18.8	9.6	5.7	2.9	19.2	20.8	98.6
Heat-treated alloy specimens										
Eutectic (peritectic) γ′ phase	8.2	2.2	8.2	66.3	0.4	1.3	6.9	5.5	1.1	100.1
Carbide phases:										
1	0.1	0.4	1.0	4.6	–	39.4	46.2	1.1	–	92.8
3	0.3	4.4	4.9	16.7	2.6	0.9	0.7	33.5	33.2	97.2

* According to EPMA data.

Table 4. Local chemical composition* and the dendrite segregation coefficients of alloying elements in the single crystals of the as-cast and heat-treated ZhS32-VI alloy

Object of analysis and K_s	Element content, wt %, and its K_s								
	Al	Cr	Co	Ni	Mo	Nb	Ta	W	Re
As-cast alloy specimens									
Primary dendrite arm	4.8	4.8	11.6	56.3	0.9	0.6	3.1	11.7	5.3
Interdendrite region	6.9	5.8	10.6	58.8	1.3	1.7	4.5	7.5	3.0
K_s	1.2	1.2	−1.1	–	−1.4	2.8	1.5	−1.6	−1.8
Alloy specimens after homogenizing annealing									
Primary dendrite arm	5.8	5.1	11.0	57.6	1.0	0.9	3.6	10.2	4.8
Interdendrite region	6.2	5.1	10.9	59.1	1.1	1.2	4.1	8.6	3.5
K_s	1.1	1.0	−1.0	–	1.0	1.3	1.1	−1.2	−1.4

* According to EPMA data.

ZhS32-VI superalloy single crystals. It is seen that some alloying elements (Ta, Nb, Al, Cr, Mo) enrich the interdendrite regions (their $K_s > 1$) and others (W, Re, Co) demonstrate the inverse segregation ($K_s < −1$). Similar regularities of the dendrite segregation of the alloying elements were obtained when studying the

Table 5. Phase transformation temperatures in NSs

Alloy	T_{cd}	T_{eu}	T_S	T_L	T_s	T_{MC}
ZhS32-VI	1282	1305	1316	1394	1379	1345
ZhS32U	1285	1308	1334	1430	1390	1374

T_{cd} is the complete dissolution temperature of the γ′ phase in the γ solid solution (γ solvus), T_{eu} is the temperature of the onset of melting of the eutectic γ′ phase, T_S is the solidus temperature, T_L is the liquidus temperature, T_s is the temperature of the onset of melt solidification, ands T_{MC} is the temperature of the onset of formation of carbides during solidification.

ZhS32U superalloy and also in [9, 21−23] for the second- and third-generation single-crystal NSs.

The chemical microheterogeneity of the structure of the as-cast single crystals of the alloys under study predetermines the temperature ranges of the main phase transformations in the ZhS32-VI and ZhS32U superalloys, such as the dissolution of hardening γ′-phase particles in the γ solid solution, melting of the eutectic (peritectic) γ′ phase and the matrix γ solid solution, melt solidification, and carbide formation. Table 5 lists these phase transformation temperatures. Based on these data, we choose the conditions of heat treatment of the ZhS32-VI and ZhS32U superalloys single crystals, in particular, the homogenization temperature.

Figure 3 shows the typical microstructure of the ZhS32-VI superalloy in single-crystal ingots with ⟨001⟩ and ⟨111⟩ CGOs after homogenizing annealing at a temperature of 1280°C. The dispersed γ′-phase
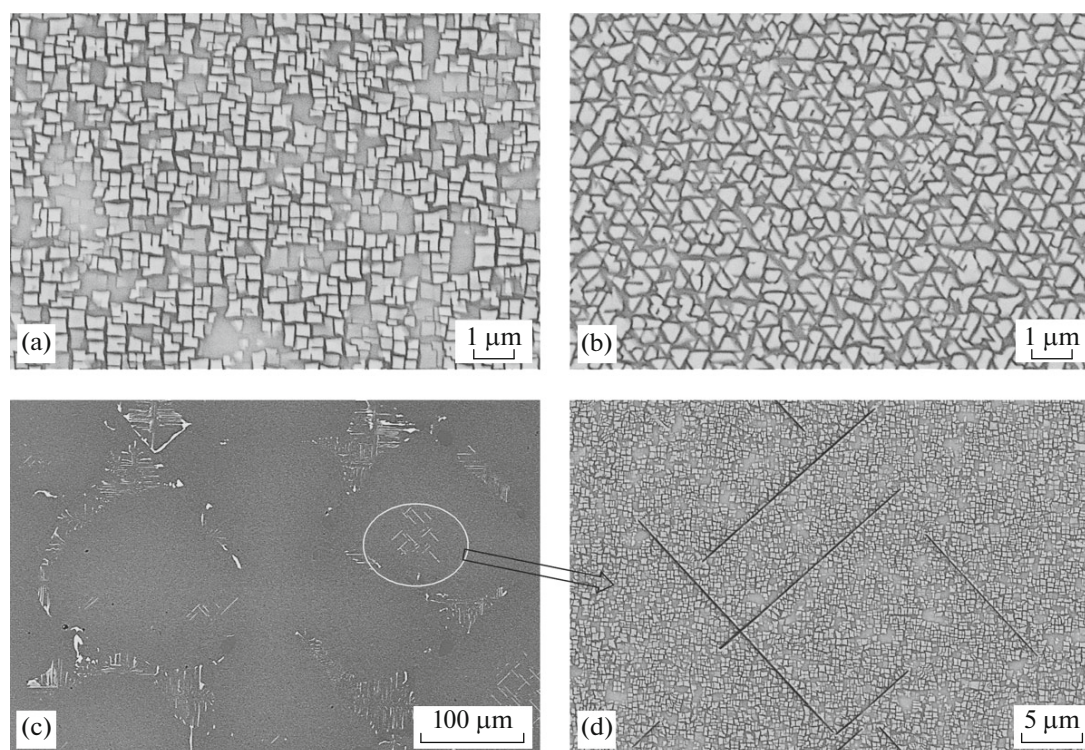
Fig. 3. Microstructure of the ZhS32-VI superalloy single crystal after heat treatment at 1280°C (cross section): (a, b) shapes and distributions of γ′-phase particles in matrix γ solid solution of superalloy single crystals with orientations (a) ⟨001⟩ and (b) ⟨111⟩; (c, d) lamellar precipitates of the M_6C carbide phase in the secondary dendrite arms.

particles formed during the decomposition of the γ solid solution on cooling from the homogenizing temperature acquire plane surface faceting, have the same sizes, and remain coarser in the interdendrite regions. This is a result of incomplete homogenization of rhenium ($K_s(Re) = -1.4$), tungsten ($K_s(W) = -1.2$), and niobium ($K_s(Nb) = 1.3$) during heat treatment, while the segregation coefficients of other alloying elements are close to unity within the error of their determination (Table 4).

As a result of homogenization, the eutectic (peritectic) γ phase was partially dissolved and coarse M_6C carbide-phase particles containing in the ZhS32-VI superalloy dissolved completely. In addition, the contents of alloying elements, such as chromium, molybdenum, tungsten and nickel, in MC carbides decreased and the niobium content increased. These changes in the chemical composition of the phases in the ZhS32-VI superalloy are likely to result in the formation of a low content of lamellar particles in secondary dendrite arms (Figs. 3c, 3d); they are likely to be TCP-phase particles. However, according to the EPMA data, the chemical composition of these particles was thought to be close to the M_6C-type carbide phase (Table 3, carbide phase 2).

Table 6 gives the lattice parameters of the γ′ and γ phases of the superalloy single crystals studied in heat-treated state, which were obtained by the decom-

position of the (222) Fe(K_α) (γ + γ′) reflection into the phase γ and γ singlets. Two conclusions follow from these data. First, the ZhS32-VI and ZhS32U superalloys have positive γ/γ′ ($a_\gamma > a_{\gamma'}$) misfits of 0.13 and 0.29%, respectively. The lower misfit in the ZhS32-VI superalloy seems to be explained by a lower tungsten content in the alloy, which has a lower tungsten content. This circumstance will favor the thermal stability of the γ/γ′ microstructure due to a lower level of the interphase stresses in the ZhS32U superalloy [24]. Second, the volume fractions of the γ and γ′ phases in the superalloy can be estimated from the ratio of X-ray reflection intensities measured separately for the γ and γ′ phases. We calculated the volume fraction of the γ′ phase $F_{0_{\gamma'}}$ in the superalloys based on the obtained

Table 6. Structure-phase parameters of superalloys

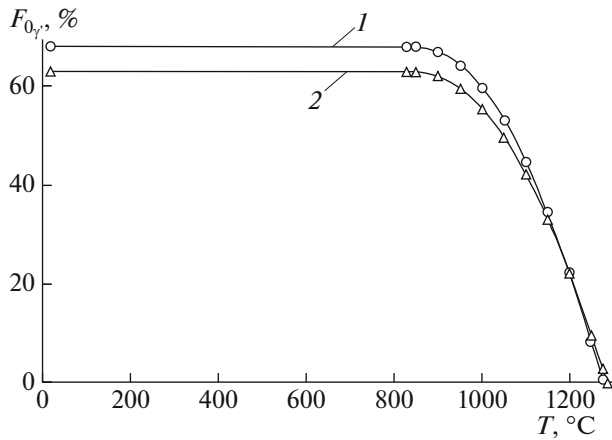| Alloy	a_γ	a_γ'	Δa	$F_{0_{\gamma'}}$
	nm		%	
ZhS32-VI	0.35985	0.35882	0.29	72
ZhS32U	0.35882	0.35832	0.13	67

The misfit estimated by Eq. (2).

Fig. 4. Temperature dependences of the γ′-phase solubility in (*1*) ZhS32-VI and (*2*) ZhS32U superalloys.

data on the decomposition of the total (γ + γ′) reflection into the phase γ′ and γ singlets using the formula [24]

$$F_{0_{\gamma'}} = I_{\gamma'}/(I_{\gamma'} + I_{\gamma}), \qquad (5)$$

where $I_{\gamma'}$ and I_{γ} are the X-ray intensities of the γ′ and γ phases, respectively. We found that the values of $F_{0_{\gamma'}}$ (Table 6) of the ZhS32-VI and ZhS32U superalloys obtained by XRD using Eq. (5) coincide quite well with the values calculated by Eq. (1).

From the calculations by Eq. (1), it follows that the volume fraction of the γ′ phase in the ZhS32-VI and ZhS32U superalloys at room temperature is 67 and 63%, respectively. From the DTA data for these superalloys on the temperatures of start (850°C) and finish (1276, 1285°C) of dissolution of the γ′ phase in the γ matrix, the temperature dependence of the volume fraction of the γ′ phase in the superalloys $F_{\gamma'}(T)$ can be calculated by the equation [25]

$$F_{\gamma'}(T) = F_{0_{\gamma'}}\left[1 - \left(\frac{T - T_0}{T_{cd} - T_0}\right)^2\right], \qquad (6)$$

where $F_{0_{\gamma'}}$ is the volume fraction of the γ′ phase at room temperature, %, and T_0 and T_{cd} are the temperatures of the start and complete dissolution of the γ′ phase (the γ′-solvus temperature), °C, respectively. Figure 4 shows the calculation results. It follows from these results that the volume fraction of the γ′ phase in the ZhS32-VI and ZhS32U superalloys at a temperature of 1150°C is ~35%.

Figure 5 shows images of the γ/γ′ microstructure of the ZhS32U superalloy after annealing at 1150°C for 660 h. During annealing at 1150°C, the γ′-phase particles of the alloy became rougher and the size of the γ solid solution interlayer between them increased. In this case, the characteristic particle size $\sqrt{S}$ (S is the particle cross-section area) in the interdendrite por-
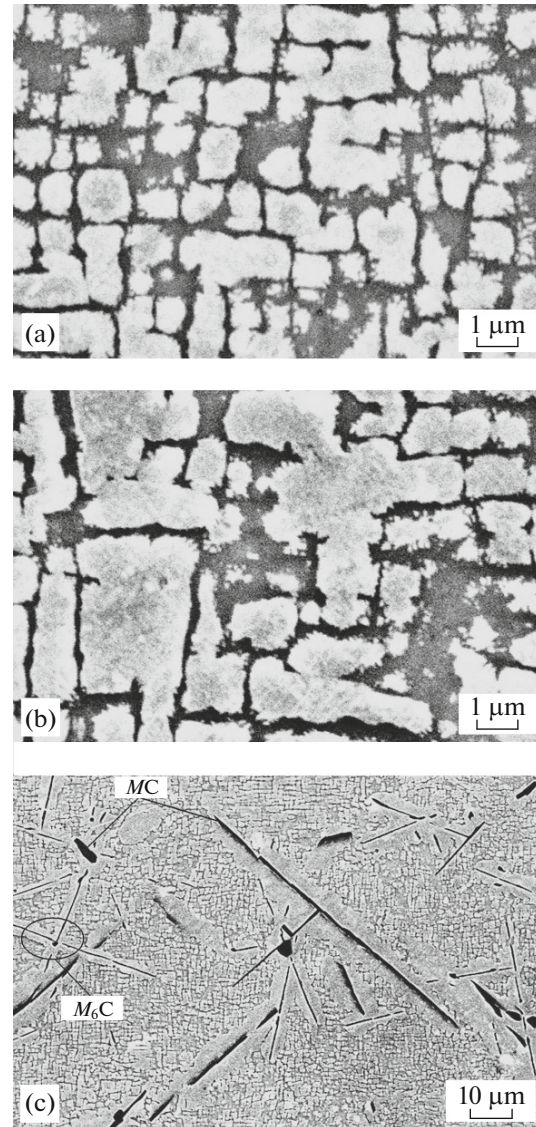

Fig. 5. Microstructure of the ZhS32U superalloy single crystal after annealing at 1150°C for 660 h: (a, b) γ′-phase particles in (a) γ matrix of primary dendrites and (b) interdendrite regions; (c) precipitates of (thick black plates) MC carbides and (thin black plates) M_6C carbides surrounded by a γ′-phase shell.

tions of the single crystal is nearly twice as large as that in dendrite arms. Comparing the microstructures shown in Figs. 5a and 5b, we can conclude that the rate of roughening of the γ′-phase particles $d\sqrt{S}d\tau$ (τ is time) of the superalloy in the interdendrite particles is nearly twice as high as that in dendrites. A similar difference in the rates of microstructure transformations is a result of lower rhenium and tungsten concentrations in the interdendrite portions as compared to those in dendrites because of incomplete homogenization of these elements during heat treatment (Table 4).

Table 7. Elastic moduli of NS single crystals with different axial CGOs

Alloy	CGO	E, GPa, at temperature, °C					Source
		20	700	800	900	1000	
ZhS32-VI	⟨001⟩	129.0	–	–	–	–	This work
	⟨111⟩	335.0	–	–	–	–	
ZhS32U	⟨001⟩	125.0	104.0	98	92	85.0	
	⟨011⟩	225.0	188.0	180	171	162.0	
	⟨111⟩	312.0	265.0	256	246	235.0	
ZhS6F	⟨001⟩	137.5	–	–	–	95.0	[13]
	⟨011⟩	234.9	–	–	–	169.7	
	⟨111⟩	307.8	–	–	–	188.2	
ZhS36	⟨001⟩	138.9	110.0	–	–	98.0	[27]
	⟨011⟩	240.5	194.0	–	–	–	
	⟨111⟩	318.0	271.7	–	–	–	
VZhM4	⟨001⟩	130.0	101.0	94	92	86.0	[28]
	⟨011⟩	233.0	184.0	175	164	156.0	
	⟨111⟩	300.0	240.0	233	213	199.0	
CMSX-4*	⟨001⟩	128.0	–	99	94	87.0	[29]
	⟨011⟩	226.0	–	182	174	164.0	
	⟨111⟩	313.0	–	257	245	239.0	

* According to the data presented in [29].

Along with roughening of the γ′ phase during annealing, we also observed the formation of new thin-lamellar phase precipitates (wide and thin lamellar precipitates in Fig. 5c) near MC carbides. According to the EPMA data, these precipitates should be supposedly referred to MC carbide phases, and the shell (bright regions around plates in Fig. 5c) formed around the plates had the chemical composition corresponding to the γ′-phase composition.

It should be noted that physicochemical phase analysis [26] showed the formation of the M_6C carbide phase in the ZhS32 superalloy with a chemical composition close to that of the ZhS32U superalloy studied in this work during long-term annealing in the temperature range 850–1250°C. However, no TCP phase formation in the ZhS32 superalloy was observed. It seems likely that the phase reactions with the precipitation of lamellar M_6C carbides were the main reactions during prolonged high-temperature

holding and proceeded according to the well-known formula γ + MC → γ′ + M_6C.

Tensile Properties of the Alloys

The results of processing of the tensile stress–strain curves measured during tensile tests of single crystals of the ZhS32-VI and ZhS32U superalloys with ⟨001⟩, ⟨011⟩, and ⟨111⟩ CGOs are presented in Table 7 and Fig. 6. The static elastic moduli of the single crystals of the ZhS32-VI and ZhS32U superalloys agree quite well with the available data [13, 27–29] for NS single crystals with the carbide–intermetallic hardening (ZhS6F) and rhenium-containing NSs with intermetallic hardening (ZhS36, VZhM4, and CMSX-4; see Table 7).

Over the entire temperature range under study, the highest elastic modulus E was observed in the NS single crystals with orientation ⟨111⟩, and the lowest mod-
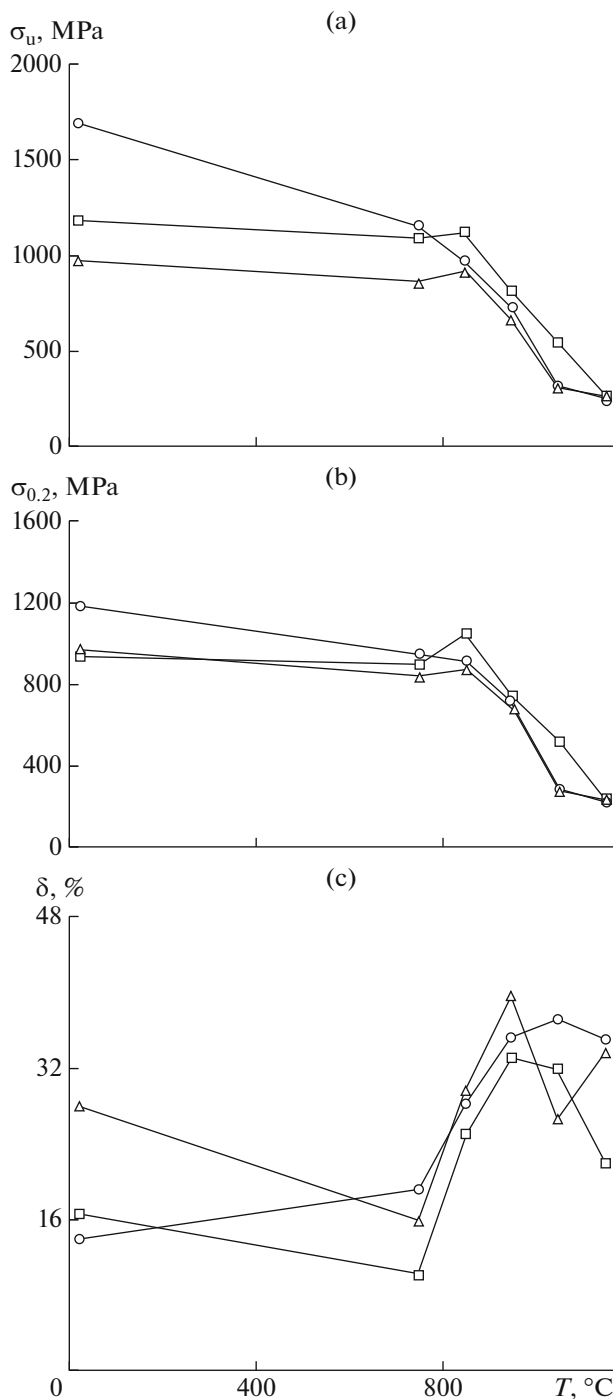
Fig. 6. Temperature–orientation dependences of (a) ultimate strength σ_u, (b) yield strength $\sigma_{0.2}$, and (c) relative elongation δ of ZhS32U superalloy single crystals with orientations ($\square$) $\langle 001 \rangle$, ($\triangle$) $\langle 011 \rangle$, and ($\bigcirc$) $\langle 111 \rangle$.

of the data on the elastic modulus of the single crystals of nickel-based superalloys of the alloying systems indicated in Table 7 showed that all of them had similar temperature−orientation dependences with an insignificant difference in magnitude within the same orientation.

As follows from the data presented in Fig. 6, ultimate strength σ_u and yield strength $\sigma_{0.2}$ of the ZhS32U superalloy single crystals with $\langle 001 \rangle$ and $\langle 011 \rangle$ CGOs had weak temperature dependences in the temperature range 20−750°C and had maxima at 850°C; the single crystal strengths decreased with a further increase in temperature. The strength of the single crystals with $\langle 111 \rangle$ CGO decreased monotonically as temperature increased, and their strengths were higher than those of the single crystals with $\langle 001 \rangle$ and $\langle 011 \rangle$ CGOs in the temperature range 20−750°C.

At higher temperatures, the short-time strength anisotropy practically degenerated, and the single crystals of all the orientations had nearly the same strength at temperatures higher than 900°C. Qualitatively similar temperature−orientation dependences of the strength characteristics were obtained earlier for ZhS6F, ZhS32 [13], and VZhM4 NS single crystals [28].

Figure 6c shows the temperature dependences of relative elongation δ of the ZhS32U superalloy single crystals of three orientations. As temperature increased, this plasticity characteristic decreased to the minimal values (12−18%) at a temperature of 750°C and substantially increased at higher temperatures. A similar plasticity dip at moderate temperatures (700−800°C) is typical of all NSs with the only difference that the minimal plasticity depended on the alloying system [13].

Low-Cycle Fatigue

Figure 7 shows the results of LCF tests at 850°C of the ZhS32U single crystals of three orientations in the $\Delta \varepsilon - \log N$ semilogarithmic coordinates. As a result of processing of the experimental LCF data, we calculated coefficients B and β in Eq. (3), from which the strain ranges $\Delta \varepsilon$ were determined at $N = 10^4$ cycles for the superalloy single crystals with orientations $\langle 001 \rangle$ and $\langle 011 \rangle$, and $\langle 111 \rangle$; the results are given in Table 8. According to these data, orientation $\langle 001 \rangle$ was more preferable for the ZhS32U superalloy for the LCF resistance under hard loading conditions at 850°C and 10^4 cycles. In this case, the lowest results were obtained for orientation $\langle 111 \rangle$. A qualitatively similar character of the influence of CGO on the LCF characteristics of the single crystals were obtained for rhenium-containing NSs with intermetallic hardening of DD6 alloy at 760°C [30, 31] and a nickel-based VKNA intermetallic alloy at 850°C [32].
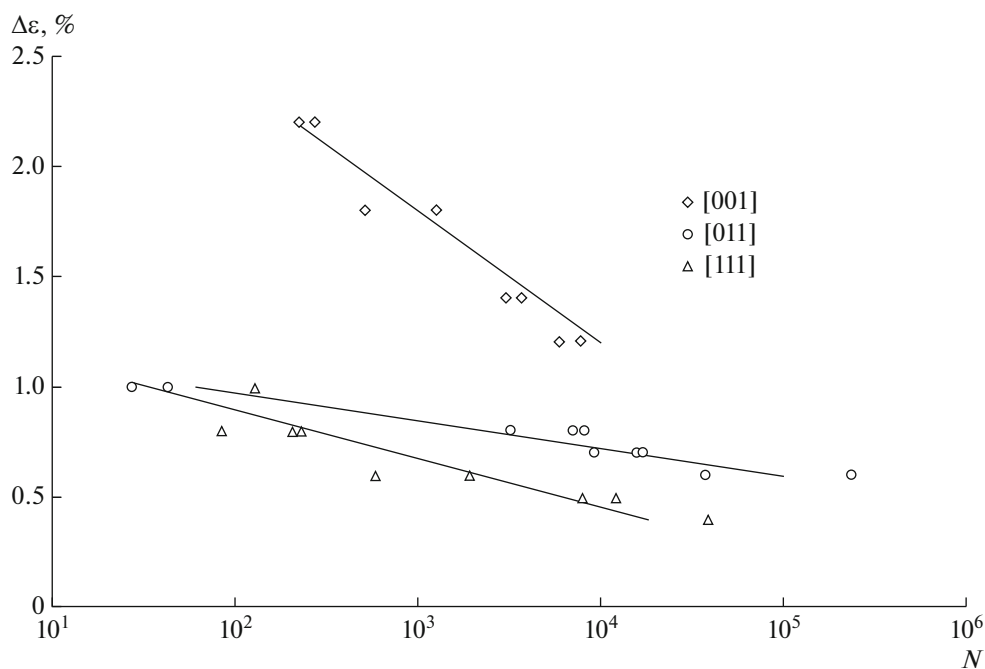
ulus was observed in the single crystals with orientation $\langle 001 \rangle$. In this case, the static elastic modulus monotonically decreased as temperature increased irrespective of CGO in single crystals. A comparison

Fig. 7. Low-cycle fatigue curves measured at a temperature of 850°C for ZhS32U superalloy single crystals with CGO $\langle 001 \rangle$, $\langle 011 \rangle$, and $\langle 111 \rangle$ (N is the number of cycles to failure).

During LCF tests of the ZhS32U single crystals at 850°C, we determined the nonstatic elastic moduli from the slopes of hysteresis loops in the elastic region during the first half-cycle at the same loading rate. Their values for orientations $\langle 001 \rangle$ ($E = 100$ GPa), $\langle 011 \rangle$ ($E = 177$ GPa), and $\langle 111 \rangle$ ($E = 250$ GPa) correlate well with the data on the static elastic moduli of single crystals of this superalloy (Table 7).

CONCLUSIONS

(1) During directional solidification of single crystals with axial $\langle 001 \rangle$, $\langle 011 \rangle$, and $\langle 111 \rangle$ CGOs of rhenium-containing nickel-based ZhS32-VI and ZhS32U superalloys, the segregation of alloying elements took place; it led to their nonuniform distribution over dendrite cells in the single crystals (Al, Cr, Mo, Ta, and Nb enrich the interdendrite regions; W, Re, and Co concentrate in dendrite arms). As a result, we produced single-crystal ingots with a dendritic–cellular structure, which consisted of primary and secondary γ/γ' dendrite arms between which precipitates of an MC-type carbide and the eutectic (peritectic) γ' phases were disposed. Homogenizing annealing at a temperature of 1280°C decreased the segregation coefficients of a number of alloying elements (Al, Cr, Mo, Co) to an equilibrium value of ± 1; in this case, no complete homogenization of tungsten, rhenium, and niobium was achieved.

(2) We found the phase transformation temperatures in the ZhS32-VI and ZhS32U superalloys on heating and cooling and an analytical form for the temperature dependence of the solubility of the γ' phase in the γ solid solution of the alloys.

(3) It was found that the ZhS32U and ZhS32-VI superalloys had positive ($a_\gamma > a_{\gamma'}$) γ/γ' lattice misfits of 0.13 and 0.29%, respectively.

(4) It was found that homogenization at 1280°C of ZhS32-VI superalloy single crystals and prolonged (for ~700 h) annealing of ZhS32U superalloy single crystals led to the formation of a small amount of lamellar particles of supposedly an M_6C carbide phase.

(5) The anisotropy of the static elastic moduli of the ZhS32-VI and ZhS32U superalloys single crystals with axial $\langle 001 \rangle$ and $\langle 011 \rangle$, and $\langle 111 \rangle$ CGOs is conserved over the entire temperature range 20–1000°C; in this case, the single crystals with orientation $\langle 111 \rangle$ had the

Table 8. Coefficients of Eq. (3) and the peak-to-peak strain at $N = 10^4$ cycles for ZhS32U superalloy single crystals, according to LCF tests at 850°C

CGO	log$B$	β	$\Delta\varepsilon$, %
$\langle 001 \rangle$	−1.59	5.89	1.20
$\langle 011 \rangle$	−8.03	9.81	0.72
$\langle 111 \rangle$	−4.61	6.10	0.46

maximum elastic modulus and the single crystals with CGO $\langle 001 \rangle$ had the minimum elastic modulus.

(6) A substantial anisotropy of the strength and plasticity characteristics of ZhS32U superalloy single crystals was observed only to a temperature of 750°C; above 900°C, the alloy single crystals of three CGOs had nearly the same strengths. At 850°C, the strength of the single crystals with $\langle 001 \rangle$ and $\langle 011 \rangle$ CGOs was maximal, and the plasticity was minimal at 750°C. The strength of the single crystals with $\langle 111 \rangle$ CGO decreased monotonically as temperature increased in the range 20−1150°C.

(7) Under conditions of hard loading cycle, the maximum LCF resistance at a temperature of 850°C and 10^4 cycles was obtained for ZhS32U single crystals with $\langle 001 \rangle$ CGO and the minim resistance was found for $\langle 111 \rangle$ single crystals.

ACKNOWLEDGMENTS

REFERENCES

1. S. T. Kishkin and E. N. Kablov, "Cast high-temperature superalloys for turbine blades," in *Aviatsionnye Materialy* (MISiS−VIAM, Moscow, 2002), pp. 48−58.

2. *Cast Blades of Gas-Turbine Engines. Alloys, Technologies, and Coatings*, 2nd ed., Ed. by E. N. Kablov (Nauka, Moscow, 2006).

3. C. S. Wukusick and L. Buchakjian, "Improved property-balanced nickel-base superalloys for producing single crystal articles: René N5." GB Patent 2235697, 1991.

4. W. S. Walston, K. S. O'Hara, E. W. Ross, T. M. Pollock, and W. H. Murphy, "René N6: Third generation single crystal superalloy," in *Superalloys 1996* (Champion, Pennsiylvania, 1996), pp. 27−34.

5. K. Harris and L. Erickson, "Low carbon directional solidification alloy CM186LC," US Patent 5069873, 1991.

6. C.-Y. Jo, N. Jones, S.-J. Choe, and D. Knowles, "High temperature mechanical properties and creep crack initiation of DS CM186LC for nozzle guide vane," Metals Materials **4** (5), 1017−1025 (1998).

7. I. M. Wilcock, P. Lukas, M. Maldini, J. Klabbers, B. Dubiel, and M. B. Henderson, "The creep behavior of as-cast SX CM186LC at industrial gas turbine operating conditions," in *Proceedings of the 7th Liège Conference on Materials for Advanced Power Engineering 2002*" (Forshungszentrum Jülich GmbH, 2002), Vol. 1, pp. 139−147.

8. E. N. Kablov and E. P. Golubovskii, *High-Temperature Strength of Nickel-Based Superalloys* (Mashinostroenie, Moscow, 1998).

9. E. N. Kablov, N. V. Petrushin, M. B. Bronfin, and A. A. Alekseev, "Specific features of rhenium alloyed single-crystal nickel superalloys," Russian Metallurgy (Metally), No. 5, 406−414 (2006).

10. A. Mottura and R. C. Reed, "What is the role rhenium in single crystal superalloys?" in *Eurosuperalloys 2014*. http://www.matec-conferences.org.

11. B. Seiser, R. Drautz, and D. G. Pettifor, "TCP phase predictions in Ni-based superalloys: structure maps revisited," Acta Materialia **59**, 749−763 (2011).

12. *Superalloys II: High-Temperature Materials for Aerospace and Industrial Power Plants* (Metallurgiya, Moscow, 1995), Vol. 1.

13. P. E. Shalin, I. L. Svetlov, E. B. Kachanov, V. N. Toloraiya, and O. S. Gavrilin, *Nickel Superalloy Single Crystals* (Mashinostroenie, Moscow, 1997).

14. V. N. Toloraiya, E. N. Kablov, and N. G. Orekhov, "Technology of casting of single-crystal turbine blades of GTE and GTU," Aviatsionnye Materialy Tekhnologii, No. 1, 63−79 (2003).

15. E. W. Ross and K. S. O'Hara, "RENÉ N4: a first generation single crystal turbine airfoil alloy with improved oxidation resistance, low angle boundary strength and superior long time rupture strength," in *Superalloys 1996* (Champion, Pennsiylvania, 1996), pp. 19−25.

16. E. N. Kablov, "Innovation developments of FGUP GNTs RF VIAM on organization of "Strategic directions of the development of materials and technologies of their reprocessing in the period to 2030," Aviatsionnye Materialy Tekhnologii, No. 1 (34), 3−33 (2015).

17. A. V. Belikov, T. S. Sinichkina, and E. M. Visik, "An UVNK unit for casting of high-temperature alloys (review)," Trudy VIAM, No. 12, St. 2 (2014) (viam-works.ru).

18. E. N. Kablov and N. V. Petrushin, "Computer method of designing casting high-temperature nickel-based superalloys," in C*ast High-Temperature Superalloys. The Kishkin Effect*, Ed. by E. N. Kablov (Nauka, Moscow, 2006), pp. 56−78.

19. M. S. Belyaev, K. K. Khvatskii, and M. A. Gorbovets, "Comparative analysisof the Russian and foreign standards of fatigue tests of metals," Trudy VIAM, No. 9, St. 11 (2014) (viam-works.ru).

20. E. P. Golubovskii, I. L. Svetlov, N. P. Petrushin, S. A. Cherkacova, and M. E. Volkov, "Low-cycle fatigue of single-crystals of high-temperature nickel-based superalloys at high temperatures," Deform. Razrushenie Mater., No. 8, 41−48 (2009).

21. A. I. Epishin, I. L. Svetlov, N. V. Petrushin, Yu. V. Loshchinin, and T. Link, "Segregation in single crystal nickel-base superalloys," Defect and Diffusion Forum **309−310**, 121−126 (2011).

22. T. M. Pollock, "Nickel-based superalloys for advanced turbine engines: chemistry, microstructure, and properties," J. Prop. Power **22** (2), 361−374 (2006).

23. B. H. Ge, Y. S. Luo, J. R. Li, and J. Zhu, "Distribution of rhenium in a single crystal nickel-based superalloy," Scripta Materialiya **63**, 969−972 (2010).

24. A. I. Samoilov, R. M. Nazarkin, N. V. Petrushin, and N. S. Moiseeva, "Misfit as a characteristic of the level of interfacial stresses in single-crystal nickel superalloys," Russian Metallurgy (Metally), No. 5, 411−417 (2011).

25. A. I. Epishin, N. V. Petrushin, T. Link, G. Nel'tse, Yu. V. Loshchinin, and G. Gerstein, "Study of the thermal stability of the structure of a cobalt high-temperature alloy with intermetallic-compound hardening of the γ phase," Deform. Razrushenie Mater., No. 3, 17−22 (2015).

26. G. D. Pigrova and A. I. Rybnikov, "Carbide phases in the ZhS32 superalloy," Mech. Term. Obrab. Met., No. 12 (702) 21−23 (2013).

27. V. G. Seleznev, M. A. Rozanov, and N. I. Minova, "Determination of physical characteristics of the single-crystal ZhS36 superalloy," in *New Technological Processes and Reliability of GTE*. Vol. 7. *Provision of the Strength Reliability of Working Blades of High-Temperature Turbines* (TsIAM, Moscow, 2008), pp. 73−77.

28. E. N. Kablov, N. V. Petrushin, I. L. Svetlov, and I. M. Demonis, "New-generation nickel-based cast high-temperature superalloys," Aviatsion Mater. Tekhnologii, No. S (Special issue), 36−52 (2012).

29. M. Fährmann, W. Hermann, E. Fährmann, A. Boegil, T. M. Pollock, and H. G. Sockel, "Determination of matrix and precipitate elastic constants in (γ–γ) Ni-based model alloys, and their relevance to rafting," Mater. Sci. Eng. A **60** (1−2), 212−221 (1999).

30. W. Yun-Jiang and W. Chong-Yu, "First principles calculation for the elastic properties of Ni-base model superalloys: Ni/Ni$_3$Al multilayers," Chin. Phys. B **18** (10), 4339−4348 (2009).

31. D. Shi, J. Huang, X. Yang, and H. Yu, "Effects of crystallographic orientations and dwell types on low cycle fatigue and life modeling of a SC superalloy," Intern. J. Fatigue **49**, 31−39 (2013).

32. M. A. Gorbovets, O. A. Bazyleva, M. S. Belyaev, and I. A. Khodinev, "Low-cycle fatigue of single-crystal VKNA intermetallic superalloy under conditions of "hard" loading," Metallurg, No. 8, 111−114 (2014).

Translated by Yu. Ryzhkov